



## Photocatalysis removing of NO based on modified carbon nitride: The effect of celestite mineral particles

Guohui Dong<sup>a,\*</sup>, Liaoliao Zhao<sup>a</sup>, Xiaoxia Wu<sup>b</sup>, Mingshan Zhu<sup>c,\*</sup>, Fu Wang<sup>b,\*</sup>

<sup>a</sup> School of Environmental Science and Engineering, Shaanxi University of Science and Technology, Xi'an, 710021, China

<sup>b</sup> School of Environmental Science and Engineering, Shanghai Jiao Tong University, 800 Dongchuan Road, Shanghai, 200240, China

<sup>c</sup> Guangdong Key Laboratory of Environmental Pollution and Health, School of Environment, Jinan University, Guangzhou, 510632, China



### ARTICLE INFO

**Keywords:**  
NO removal  
Photocatalysis  
Mineral particles  
Celestite  
g-C<sub>3</sub>N<sub>4</sub>

### ABSTRACT

Atmospheric NO is one of the toxic and hazardous gases. Its' levels are continually rising in recent years. As we known, mineral particles contained in the atmosphere may affect the photocatalytic NO removal process. In this study, we found that celestite modification could greatly improve the activity (about 3.8 times) and stability of g-C<sub>3</sub>N<sub>4</sub> for the photocatalytic NO removal. In our system, celestite particles embed in the N vacancies of g-C<sub>3</sub>N<sub>4</sub>. The synergistic effect of celestite and N vacancy is the origin of improved NO removal activity. During the light irradiation, photogenerated electrons can be captured and confined by N vacancy. Meanwhile, celestite can transfer these confined electrons to O<sub>2</sub> and produce more ·OH, which could oxidize NO to nitrate. These findings can help us to understand the influence of mineral particles in the photocatalytic NO removal and design highly efficient NO removal photocatalysts.

### 1. Introduction

Acid rain, ozone depletion and photochemical smog are major global air pollution problems caused by the common source, nitrogen oxide (NO<sub>x</sub>; 95% in the form of NO) [1,2]. Atmospheric NO levels are continually rising due to increasing numbers of vehicles and industrial activities [3,4]. Atmospheric NO can trigger serious respiratory diseases, making the removal of it become a critical global concern and increasing the need for efficient and economical removal technology [5–7]. Among the various atmospheric NO removal strategies, photocatalytic technology is a cost-effective and environmentally-friendly technology that utilizes solar energy [8–10]. Among various photocatalysts, graphite carbon nitride (g-C<sub>3</sub>N<sub>4</sub>) is a promising visible-light sensitive and metal-free photocatalyst, which has attracted increasing attention because of its low cost, high stability and special optical features [11–13]. However, for pure g-C<sub>3</sub>N<sub>4</sub>, the removal activity is low due to the fast recombination of photo-generated carriers [14]. Additionally, g-C<sub>3</sub>N<sub>4</sub> photocatalysis for NO removal generates NO<sub>2</sub> as the main product, which is more toxic than NO [14]. As we known, the complete oxidation product of NO is HNO<sub>3</sub>. Therefore, the NO removal on pure g-C<sub>3</sub>N<sub>4</sub> is an incomplete oxidation process. The incomplete oxidation is due to the fact that g-C<sub>3</sub>N<sub>4</sub> system cannot produce the strong oxidizing ·OH. This fact has two reasons as follow: One is that the valence band holes (1.4 eV) are not positive enough to oxidize OH<sup>−</sup>

to ·OH (2.3 eV) [11]; the other is that the H<sub>2</sub>O<sub>2</sub> generated through the reduction of conduction band electron cannot be activated to ·OH on the surface of g-C<sub>3</sub>N<sub>4</sub> [15]. Therefore, there is an urgent need to develop new kind of g-C<sub>3</sub>N<sub>4</sub>-based materials for absolutely removal of NO.

In addition to gases, the atmosphere also contains small mineral particles [16]. Because of their high surface energy and the free radical properties of NO, NO are likely to be adsorbed on mineral particle surfaces. As mineral particles play an important role in photochemical reaction of NO, it is likely that modification with mineral nanoparticles may improve the NO removal activity of g-C<sub>3</sub>N<sub>4</sub>. In addition, mineral nanoparticles contain variable valence metal ions (V-VMI), which may improve the activity of photocatalyst. Firstly, V-VMI can capture photo-generated electrons and thus inhibit the recombination of photo-generated carriers [17]. Then, V-VMI could decompose H<sub>2</sub>O<sub>2</sub> into ·OH via a Fenton like reaction, and ·OH is a strong oxidizer can oxidize NO to nitrate [18].

Celestite is a crystal of strontium sulfate (SrSO<sub>4</sub>), which is the principal source of strontium (Sr), an essential trace element in the human body [19]. Sr ions in celestite have empty orbitals, which may help photocatalysts absorb more oxygen through coordination bonds, and thus photocatalyst may produce more reactive oxygen species. In addition, SO<sub>4</sub><sup>2−</sup> ions may increase surface acidity and consequently increase the NO adsorption capacity of photocatalyst, increasing NO removal activity significantly. Therefore, a systematic assessment of the

\* Corresponding authors.

E-mail addresses: [dongguohui@sust.edu.cn](mailto:dongguohui@sust.edu.cn) (G. Dong), [mingshanzhu@yahoo.com](mailto:mingshanzhu@yahoo.com) (M. Zhu), [wangfu@sjtu.edu.cn](mailto:wangfu@sjtu.edu.cn) (F. Wang).

effect of celestite on NO removal behavior of  $\text{g-C}_3\text{N}_4$  is of great importance.

In this study, we found that celestite modification could greatly improve the activity and stability of  $\text{g-C}_3\text{N}_4$  photocatalytic NO removal, under visible light irradiation. We found that celestite modification has two advantages: (1) the cost of celestite is only about 0.6 USD per kilogram, which is far lower than the cost of noble metals such as Pt and Ag (32543 and 566 USD per kilogram, respectively.); (2) celestite modification not only can improve the NO removal activity of  $\text{g-C}_3\text{N}_4$  about 3.8 times, but also can change the incomplete removal to the complete removal by introducing the Fenton-like reaction. These two advantages benefit from the synergistic effect between celestite and N vacancy that caused by the heat activation of celestite. A series of experiments were designed to investigate the role of modified celestite on photocatalytic NO removal, with the reasons for enhanced activity and stability analyzed in detail.

## 2. Experimental section

### 2.1. Chemicals and Materials

All reagents employed in this study were analytical grade and used without further purification.

### 2.2. Preparation of photocatalyst

The  $\text{g-C}_3\text{N}_4$  was prepared by annealing urea under high temperature. In detail, a given amount of urea was put into a covered crucible and heated in the muffle furnace at 550 °C for 2 h with a heating rate of 10 °C/min. After cooling down to the room temperature, the product was ground into fine powder and labeled as  $\text{g-C}_3\text{N}_4$  for the further use.

Celestite (Purity: ≥ 96%) modified  $\text{g-C}_3\text{N}_4$  were prepared by annealing the mixtures of  $\text{g-C}_3\text{N}_4$  and celestite powder. Briefly, different masses (0.02, 0.05, 0.1 and 0.2 g) of celestite powder were mixed with a given amount of  $\text{g-C}_3\text{N}_4$  (1 g) and ground uniformly. Subsequently, the mixtures were placed in covered crucibles and then heated at 400 °C for 2 h. After this procedure, the crucibles were taken out and cooled to room temperature. The products were ground into fine powders and collected. Samples were labeled as CNSr-0.02, CNSr-0.05, CNSr-0.1 and CNSr-0.2, respectively.

### 2.3. Material characterization

Powder X-ray diffraction (XRD) was used for crystalline phase identification of result samples. This identification was performed on a Bruker D8 Advance diffractometer with monochromatized Cu K $\alpha$  radiation ( $\lambda = 1.5408 \text{ \AA}$ ) to get the XRD patterns. Thermal gravimetric analyzer (TGA, STA 449F3, Netzsch, Germany) was employed to test the thermal stability of different samples. UV-vis spectrometer was used to analyze the light absorption ability and band-gap of different samples. The spectra were obtained from Shimadzu UV-3700 over a range of 200–800 nm with BaSO<sub>4</sub> as a reference. Reflection spectra were converted into absorbance via the Kubelka-Munk method. Fluorescence spectrometer (Hitachi F7000) was used to study the recombination rate of photogenerated carriers in different samples. The excitation wavelength is 330 nm. Scanning electron microscopy (SEM, ZEISS SUPRA55VP) was used to observe the morphology images and elements distribution of different samples. X-ray photoelectron spectrometric (XPS) was employed to study the composition structure of different samples. It was operated on VG Scientific ESCALAB Mark II equipped with two ultrahigh vacuum chambers. An Autosorb-IQ-MP autosorption analyzer was used to analyze the Brunauer-Emmett-Teller (BET) specific surface area and pore size of different samples. Before the measurements, the samples were degassed at 373 K for 2 h and were carried out at 77.3 K using N<sub>2</sub> as an adsorbate.

### 2.4. Photocatalytic activity evaluation

The evaluation of photocatalytic performance of  $\text{g-C}_3\text{N}_4$  and CNSr-x ( $x = 0.02, 0.05, 0.1$  and  $0.2$ ) were tested by oxidation of NO at ppb levels in a continuous-flow chamber under visible light irradiation. The volume (V) of the cylindric reactor with a quartz glass on the surface was 0.785 L ( $V = \pi \times R^2 \times H$ ;  $R = 5 \text{ cm}$ ;  $H = 10 \text{ cm}$ ). For each photocatalytic activity experiment, a sample dish ( $R = 3 \text{ cm}$ ) containing the photocatalyst powders (50 mg) was placed in the center of the reactor. A 30 W LED lamp was chosen as the simulated visible light source and it was vertically placed above the reactor. The mixture gas of NO and Air were continuously passed through (1 L/min controlled by a mass flow controller) the surface of photocatalyst to reach the adsorption-desorption equilibrium and the initial concentration of NO used in the photocatalysis test was diluted to 600 ppb by air which from an air cylinder. After adsorption-desorption equilibrium among the photocatalysis, the LED lamp was switched on. The NO, NO<sub>2</sub> and NO<sub>T</sub> ( $\text{NO}_T = \text{NO} + \text{NO}_2$ ) concentrations were continuously measured by using a chemiluminescence NO analyzer (Thermo Scientific, 42i). The NO removal decrement ( $\eta$ ) was calculated by the following equation:

$$\eta = (1 - C/C_0) \times 100\%$$

where  $C_0$  represents inlet concentration after achieving adsorption-desorption equilibrium (about 600 ppb) and C is the NO concentration (ppb) in real time.

### 2.5. The detection of free radicals

A Bruker E500 instrument was used for the electron paramagnetic resonance (EPR) experiments, which was often used to detect the free radicals in reaction. Samples for EPR measurement were carried out by using DMPO (5,5-dimethyl-l-pyrroline N-oxide) as the spin trapping agent, mixing the samples (10 mg) in a 40 mM DMPO solution tank (methanol dispersion for superoxide radicals and aqueous dispersion for hydroxyl radicals) and irradiated with visible light.

### 2.6. Trapping experiments of visible-light induced active species

We used potassium iodide (KI) and potassium dichromate (K<sub>2</sub>Cr<sub>2</sub>O<sub>7</sub>) as effective scavengers of photoinduced hole and electron, respectively [20]. Tert-butyl alcohol (TBA) and p-benzoquinone (PBQ) were utilized as scavengers of hydroxyl radical (OH) and superoxide radical (O<sub>2</sub><sup>·</sup>), respectively [20]. Typically, photocatalysts (50 mg) containing different trapping agents (1 mmol) were dispersed in deionized water (10 mL) and ultrasonicated for 15 min. Then, the dispersed suspensions were poured into glass dishes and drying at 60 °C until the water was completely removed. Finally, the dried dishes were further utilized in NO removal experiments.

### 2.7. Photoelectrochemical experiments

The photoelectrochemical properties of  $\text{g-C}_3\text{N}_4$  and CNSr-x ( $x = 0.02, 0.05, 0.1$  and  $0.2$ ) were evaluated using an electrochemical workstation (CHI660C) in a three electrode quartz cells. A platinum plate ( $1 \times 1 \text{ cm}^2$ ) and a saturated calomel electrode (SCE) were used as a counter electrode and a reference electrode, respectively. To fabricate the working electrode, photocatalysts were dispersed in 1 mL of Nafion ethanol solution and ground for 10 min to obtain homogeneous slurry. The resultant slurry were loaded on the pretreated fluorine tin oxide (FTO) glasses ( $1.5 \times 1.5 \text{ cm}^2$ ) by blade coating method and then dried under ambient conditions.

In the process of experiment, the KCl aqueous solution at concentration of 0.1 M was served as the electrolyte. The prepared working electrode was positioned in the middle of the electrolyte with the glass side facing the incident light. Current-time curves were determined in a

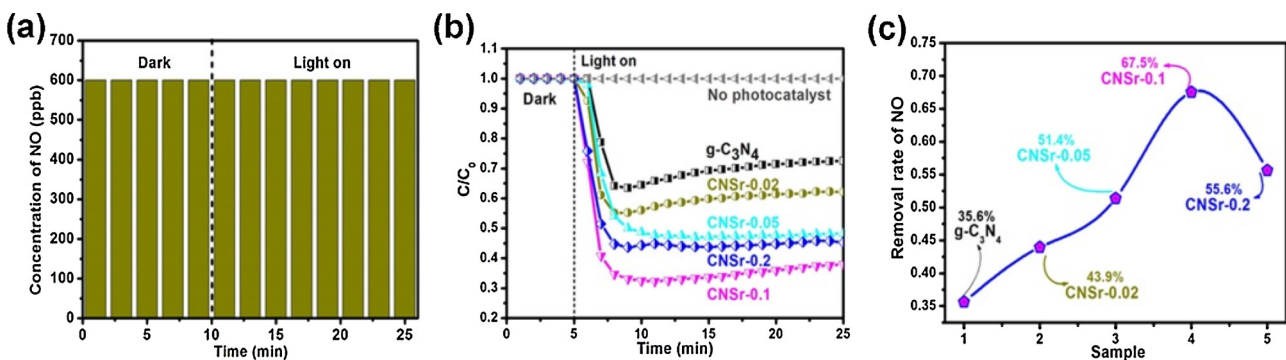


Fig. 1. Photocatalytic performance of different samples; (a) Celestite; (b) and (c) the NO removal performance of different samples.

single compartment cell with a quartz window at ambient temperature under irradiation with a 300 W Xe arc lamp.

### 3. Results and discussion

#### 3.1. Photocatalytic NO removal

Photocatalytic performance of different samples were tested under visible light irradiation, for ppb-level NO removal. Experiments were carried out at room temperature in a continuous-flow reactor cylinder, with a volume of 0.785 L, made of Pyrex glass with a quartz window. Pure celestite did not demonstrate any catalytic activity for NO removal under the same photo-irradiation conditions (Fig. 1a). When no photocatalysts or light irradiation is present, NO is stable and cannot be removed. Among the different samples tested, CNSr-0.1 exhibits optimal activity (Fig. 1b), with 67.5% of the initial NO removed after 10 min of visible light irradiation (Fig. 1c), which is higher than that of the pure g-C<sub>3</sub>N<sub>4</sub> (35.6%). Since celestite can be dissolved by diluted nitric acid, CNSr-0.1 was washed by diluted nitric acid and distilled water thoroughly to remove the modified celestite. After this washing, we found that the NO removal activity of washed CNSr-0.1 (CNSr-0.1-W) is much lower than that of CNSr-0.1 (Figure S1), suggesting the improved NO removal activity of CNSr-0.1 is caused by celestite. Because there has few impurities in celestite, we synthesized CNSr-0.1 by using SrSO<sub>4</sub> instead of celestite (Denoted as CNSr-0.1 s). The photocatalytic NO removal activity of CNSr-0.1 s is similar to that of CNSr-0.1 (Figure S2), suggesting the role of impurities in celestite is negligible. The reason may be that the concentration of impurities in celestite is very low. Meanwhile, the concentration of celestite in CNSr-0.1 is also very low. The activity of CNSr-0.1 was also compared with that of conventional material TiO<sub>2</sub> (P25). From Figure S3, the activity of CNSr-0.1 is better than that of P25. Additionally, the price of celestite (0.6 USD/Kg) is only 1/1000 or even 1/100000 of that of noble metal such as Ag (566 USD/Kg) and Pt (32,543 USD/Kg). Above results demonstrated that celestite is an inexpensive and excellent co-catalyst.

During the photocatalysis process, the concentration of NO<sub>2</sub> produced was monitored (Fig. 2a). As shown in Fig. 2b, the conversion rate of NO<sub>2</sub> in g-C<sub>3</sub>N<sub>4</sub> system was 72%, indicating the main production of NO removal in g-C<sub>3</sub>N<sub>4</sub> system is NO<sub>2</sub>. Interestingly, celestite addition can effectively reduce the conversion rate of NO<sub>2</sub> from 72% to 21%, suggesting that NO may be mainly oxidized to NO<sub>3</sub><sup>-</sup> by CNSr-0.1. The presence of NO<sub>3</sub><sup>-</sup> was confirmed by ion chromatography analysis. As shown in Fig. 2c, after undergoing the NO removal reaction, the concentration of NO<sub>3</sub><sup>-</sup> in solution was found rapidly increased in the CNSr-0.1 system. The formed NO<sub>2</sub>, and NO<sub>3</sub><sup>-</sup> can meet with the consumed NO (The calculation of N-balance can be found in supporting information). These findings indicate that the celestite can beneficially affect the NO removal process.

To further investigate the surface alterations of g-C<sub>3</sub>N<sub>4</sub> and CNSr-0.1 following the NO removal process, a series of capture experiments were

carried out. As can be seen from Fig. 3a and 3c, both KI and K<sub>2</sub>Cr<sub>2</sub>O<sub>7</sub> can significantly reduce NO removal efficiency, suggesting that photogenerated holes and electrons are both crucial to the NO removal process. The adding PBQ reduced the NO removal efficiency of both g-C<sub>3</sub>N<sub>4</sub> and CNSr-0.1, suggesting that ·O<sub>2</sub><sup>-</sup> makes a significant contribution to the NO removal process of both g-C<sub>3</sub>N<sub>4</sub> and CNSr-0.1. The addition of catalase (CAT) and tertiary butanol (TBA) clearly inhibited NO removal by CNSr-0.1, while they did not affect g-C<sub>3</sub>N<sub>4</sub>, implying that H<sub>2</sub>O<sub>2</sub> and ·OH serve different roles in g-C<sub>3</sub>N<sub>4</sub> and CNSr systems.

On the basis of above product detection and capture assay, the NO removal process by g-C<sub>3</sub>N<sub>4</sub> can be expressed chemically (Fig. 3b), by Eqs. (1)–(4) as follows:



The NO removal process by CNSr-0.1 can be expressed chemically (Fig. 3d), by Eqs. (5)–(10) as follows:



Based on the above results, we conclude that celestite not only improves the photocatalytic activity of g-C<sub>3</sub>N<sub>4</sub>, but also inhibits the generation of NO<sub>2</sub> during the NO removal process. Therefore, celestite is an effective natural co-catalyst which can facilitate the practical application of NO removal by g-C<sub>3</sub>N<sub>4</sub>.

To test the stability and practicality of different samples for NO removal, photocatalytic NO removal cycles were performed with CNSr-0.1 under fixed conditions. After undergoing 5 cycles, the NO removal capacity of CNSr-0.1 remained constant (Fig. 3e), indicating that the photocatalytic activity of CNSr-0.1 are stable with repeated use. Additionally, we compared the XRD patterns of the samples before and after photocatalytic reaction. After the photocatalytic reaction, the XRD patterns of samples have no obvious changes (Figure S4), suggesting that the structure of CNSr-0.1 are stable with repeated use.

#### 3.2. Structure analysis

The performance of catalysts is usually thought to depend on the microstructure of this catalyst. Therefore, to better understand the high

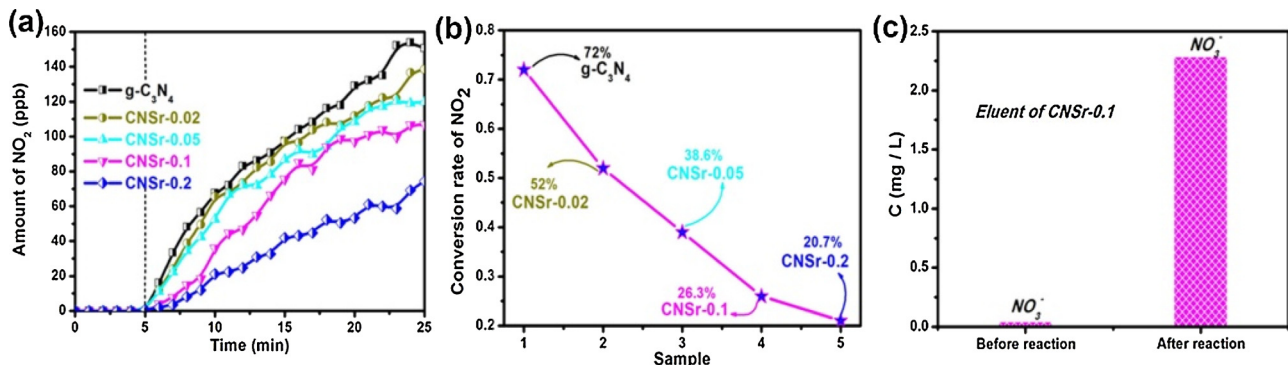


**Fig. 2.** Photocatalytic performance of different samples; (a) the amount of  $\text{NO}_2$  generated in different sample systems; (b) the conversion rate of  $\text{NO}_2$  in different sample systems; (c) the  $\text{NO}_3^-$  detected in the washing solution (concentrated 100 times) of used CNSr-0.1.

performance of CNSr-0.1, it is essential to analyze microstructure changes of CNSr-0.1, including crystallinity, chemical composition and morphology.

The XRD patterns of pure  $\text{g-C}_3\text{N}_4$ , celestite powder and CNSr-x are presented in Fig. 4. As shown by the XRD pattern of celestite powder (Fig. 4a), the XRD pattern did not contain any sharp peaks that could be assigned to  $\text{SrSO}_4$  (JCPDS no. 89-95), corresponding to the fact that celestite is a crystal of  $\text{SrSO}_4$ . As for  $\text{g-C}_3\text{N}_4$ , two distinct diffraction peaks were observed at  $27.6^\circ$  and  $13.1^\circ$ , respectively (Fig. 4b). As compared to the XRD pattern of pure  $\text{g-C}_3\text{N}_4$ , the XRD patterns of CNSr-x showed a number of new peaks that correspond to  $\text{SrSO}_4$  (Fig. 4b), suggesting that CNSr-x are composites of  $\text{g-C}_3\text{N}_4$  and celestite. More importantly, the peaks assigned to  $\text{g-C}_3\text{N}_4$  in CNSr-x became weaker, suggesting that the crystal phase of  $\text{g-C}_3\text{N}_4$  was destroyed. This phenomenon implies that celestite particles may be embedded within the structure of  $\text{g-C}_3\text{N}_4$ .

CNSr-x was synthesized by calcination of the mixture of  $\text{g-C}_3\text{N}_4$  and celestite. To determine whether  $\text{g-C}_3\text{N}_4$  and celestite could be decomposed by the calcination process, TGA analysis was carried out in a temperature range of 20–900 °C. As shown in Fig. 4c, the TGA curve for celestite showed only minor loss in temperatures above 800 °C, suggesting that celestite is stable throughout the calcination process. For pure  $\text{g-C}_3\text{N}_4$ , the mass start to decline with temperatures above 520 °C. This decline could be ascribed to the thermal decomposition of  $\text{g-C}_3\text{N}_4$ . When  $\text{g-C}_3\text{N}_4$  was mixed with celestite, the mass of samples start falling at temperatures of 350 °C and above, with this reduced decomposition temperature suggesting that celestite particles may destroy and embed in the structure of  $\text{g-C}_3\text{N}_4$  (Fig. 4d).

XPS measurements were carried out to establish the surface chemical compositions and chemical states of corresponding C, N and O elements in both pure  $\text{g-C}_3\text{N}_4$  and CNSr-0.1 (Fig. 5a). However, the O1 s spectra of different samples were analyzed, the O1 s spectra of CNSr-0.1 displayed a novel peak at 531.6 eV, in addition to the surface hydroxyl group peak observed at 532.2 eV (Fig. 5b). This novel peak was assigned to double bonded oxygen from  $\text{SO}_4^{2-}$ , indicating the presence of celestite. The presence of celestite was further confirmed by SEM images, where as compared to the  $\text{g-C}_3\text{N}_4$  nanosheets (Fig. 5c), nanoparticles (Average size: 30 nm) were found to be present on the surface of CNSr-0.1 (Fig. 5f, S6). Elemental mapping showed that both Sr and S on the surface of CNSr-0.1 (Fig. 5i and j), confirming that the nanoparticles on the surface of CNSr-0.1 are celestite. As shown in Fig. 6a and b, the C1 s and N1 s spectra of CNSr-x samples shifted to lower binding energies when compared with those of pure  $\text{g-C}_3\text{N}_4$ . The shift of these peaks to lower binding energies implies that the electron density around C and N atoms increased, indicating the interaction exists between the  $\text{g-C}_3\text{N}_4$  and celestite. Furthermore, Elemental analysis was used to study the contents of carbon and nitrogen in different samples. The content of carbon and nitrogen in  $\text{g-C}_3\text{N}_4$  sample are 36.4% and 61.1%, respectively. Meanwhile, the content of carbon and nitrogen in

CNSr-0.1 sample are 40.3% and 56.5%, respectively. The molar ratio of nitrogen to carbon (N/C) in  $\text{g-C}_3\text{N}_4$  and CNSr-0.1 are calculated as 1.5 and 1.2, respectively. Therefore, we can conclude that celestite particles induced many N vacancies in CNSr-0.1, during the calcination process.

Bridging N atoms in  $\text{g-C}_3\text{N}_4$  structures have a lone-pair of electrons, while Sr atoms in celestite have an empty 5p orbital, allowing coordination bonds to be formed between the bridging N atom of  $\text{g-C}_3\text{N}_4$  and the Sr atom of celestite. Therefore, in the mixing process of  $\text{g-C}_3\text{N}_4$  and celestite powders, celestite partials preferentially associate with bridging N atoms of  $\text{g-C}_3\text{N}_4$  because of coordination bonding. In the process of calcination, celestite partials will activate the bridging N atom, making it easier to escape from the  $\text{g-C}_3\text{N}_4$  structure. This is why celestite particles may destroy the  $\text{g-C}_3\text{N}_4$  structure, forming N vacancies. This analysis can be confirmed by the comparison of N 1 s XPS spectra. From Fig. 6b, the N 1 s spectra can be deconvoluted into two peaks at 400.3 and 398.5 eV, which correspond to the nitrogen of triazine ring and the bridging nitrogen, respectively. The area ratio of these two peaks at 400.3 and 398.5 eV were calculated to be 0.2 and 0.4 for  $\text{g-C}_3\text{N}_4$  and CNSr-x, respectively. The increase of this ratio value suggests that the concentration of bridging N atom has decreased in CNSr-0.1 samples, confirming the escape of bridging N from  $\text{g-C}_3\text{N}_4$  structure.

### 3.3. The mechanism of NO removal

With above improved understanding of the structure of  $\text{g-C}_3\text{N}_4$ , we propose that the possible origins of this improved activity include: celestite, N vacancy and the synergistic effect of celestite and N vacancy. To establish the accurate origin of the increase in activity, the NO removal activity of  $\text{g-C}_3\text{N}_4$ ,  $\text{Nv-g-C}_3\text{N}_4$  (N vacancy modified  $\text{g-C}_3\text{N}_4$ ) and celestite/ $\text{g-C}_3\text{N}_4$  (the mixture of celestite and  $\text{g-C}_3\text{N}_4$ ) were investigated. As shown in Fig. 7a, a single N vacancy did not improve the NO removal activity of  $\text{g-C}_3\text{N}_4$ , while a single celestite only slightly improved the NO removal activity of  $\text{g-C}_3\text{N}_4$ . When celestite particles embed in N vacancy, the NO removal activity of  $\text{g-C}_3\text{N}_4$  was improved significantly. These results suggest that the origin of improved activity is the synergistic effect of celestite and N vacancy.

Since photocatalytic NO removal is a surface catalytic reaction, the adsorption of reactants is an important factor in contaminant removal. A high catalyst surface area can facilitate the adsorption and mass transfer of pollutants and reaction products, therefore the increased surface area may be a key reason for the improved activity. Brunauer–Emmett–Teller (BET) gas adsorption measurements were performed to examine the surface area of pure  $\text{g-C}_3\text{N}_4$  and CNSr-0.1 samples. As shown in Fig. 7b, the pure  $\text{g-C}_3\text{N}_4$  and CNSr-0.1 sample isotherms were identified as type-IV isotherms, suggesting both samples possess mesoporous structures. Moreover, all isotherms were established as H3 hysteresis loop types, meaning that both samples were formed by aggregated nanosheets. Based on the  $\text{N}_2$  isotherms, the BET

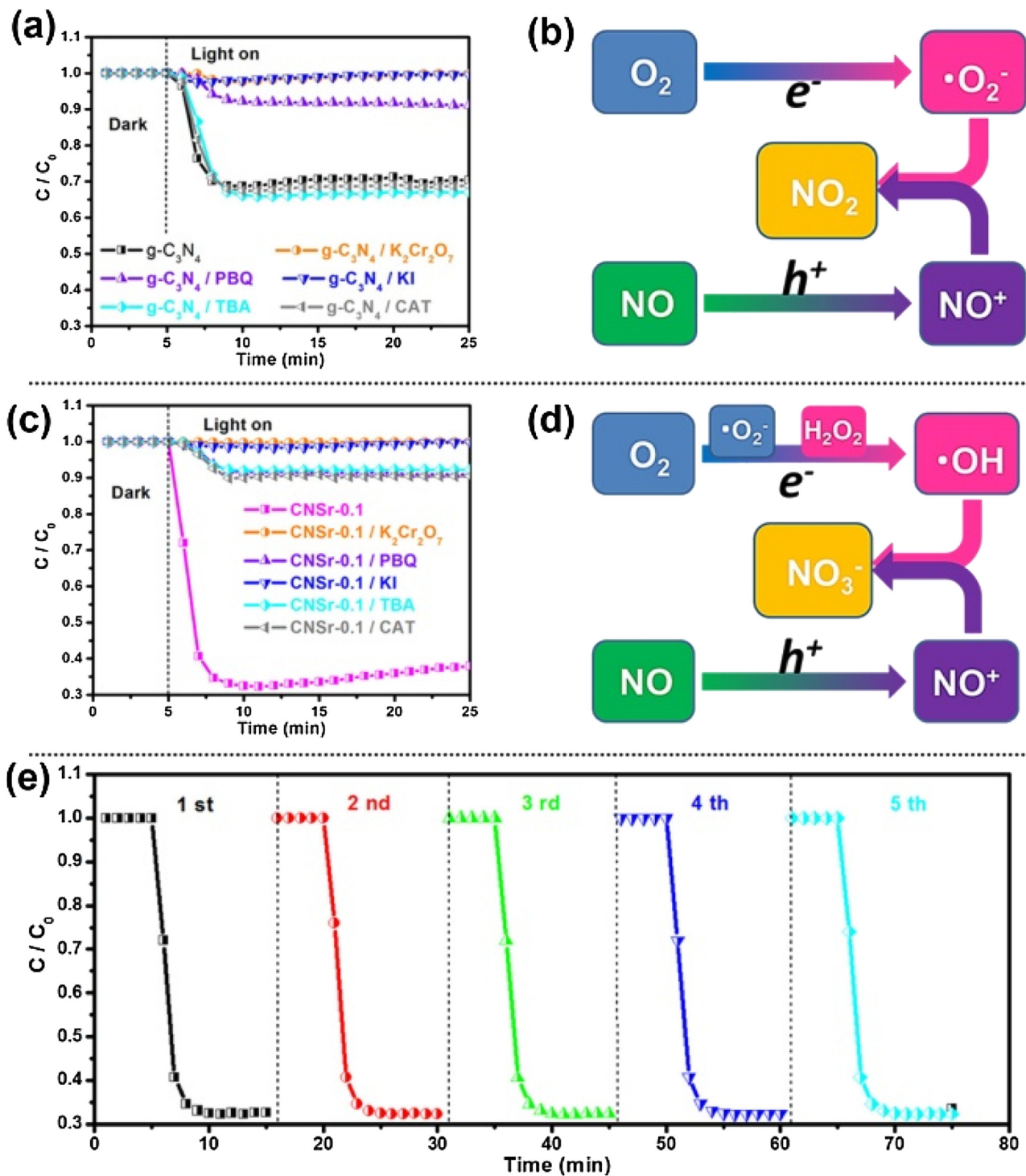


Fig. 3. (a) Capture experiments were carried out in  $\text{g-C}_3\text{N}_4$  system; (b) NO removal mechanism of  $\text{g-C}_3\text{N}_4$ ; (c) Capture experiments were carried out in CNSr-0.1 system; (d) NO removal mechanism of CNSr-0.1; (e) the stability of CNSr-0.1 for NO removal.

specific surface areas of  $\text{g-C}_3\text{N}_4$  and CNSr-0.1 were calculated to be 50.54 and  $62.71 \text{ m}^2/\text{g}$ , respectively. However, this slight increase in surface area did not match with the significant increase in photocurrent and sharp decrease in EIS.

To further reveal the reasons for the improvement in activity and any change in removal mechanisms, the light absorption performance and band gap of synthesized  $\text{g-C}_3\text{N}_4$  and CNSr-0.1 were investigated by UV-vis diffusion reflectance spectrometry (DRS). Photocatalysis processes start with light absorption and photoexcitation and as shown in Fig. 7c, a single celestite does not affect the light absorption of  $\text{g-C}_3\text{N}_4$ .

N vacancy can result in a red-shift on the absorption edges of  $\text{g-C}_3\text{N}_4$ , suggesting that the band gap of  $\text{Nv-g-C}_3\text{N}_4$  is smaller than that of  $\text{g-C}_3\text{N}_4$ . This narrowing of band gap is usually caused by the defect level, which is formed by the N vacancy [21]. It should be noted that the embedding of celestite can further aggravate the red-shift of the absorption edges of  $\text{g-C}_3\text{N}_4$ , which implies that electron transfer may occur between N vacancy and celestite.

If this speculation is accurate, celestite may also help to promote the separation and transfer of photo-generated electrons and holes. Fluorescence emission spectra allow investigation of the separation

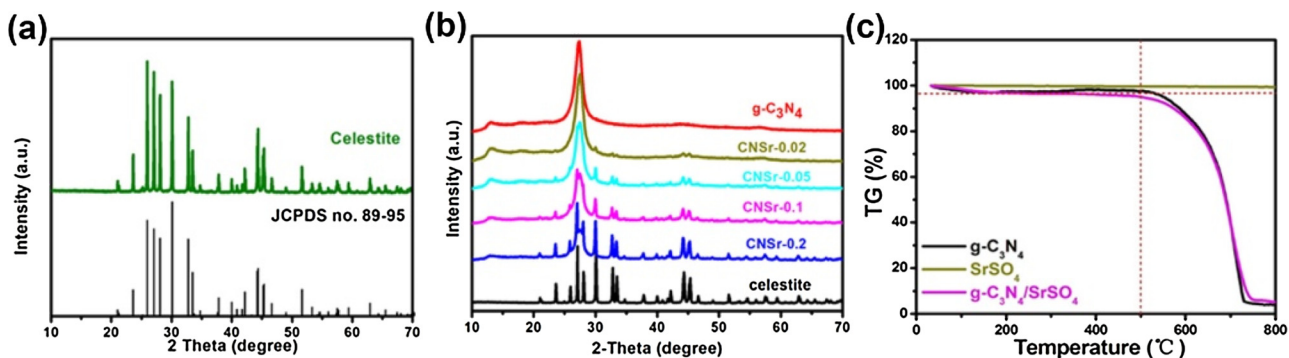


**Fig. 4.** (a) The XRD pattern of celestite powder; (b) the XRD pattern of pure  $\text{g-C}_3\text{N}_4$ , and CNSr-x samples; (c) TGA analysis was carried out in a temperature range of 20–900 °C.

efficiency of photo-generated electron-hole pairs. Fig. 7d displays the spectra at an excitation wavelength of 330 nm, of  $\text{g-C}_3\text{N}_4$ , Nv- $\text{g-C}_3\text{N}_4$ , celestite/ $\text{g-C}_3\text{N}_4$  and CNSr-0.1 samples. Generally, the photocatalyst emission peak is derived from the direct recombination of electrons and holes. Emission peaks of Nv- $\text{g-C}_3\text{N}_4$  and celestite/ $\text{g-C}_3\text{N}_4$  were found to be smaller than that of  $\text{g-C}_3\text{N}_4$ , indicating that both N vacancy and celestite could inhibit the recombination of electrons and holes. However, Nv- $\text{g-C}_3\text{N}_4$  and celestite/ $\text{g-C}_3\text{N}_4$  emission peaks were strong, compared with the emission peaks of CNSr-0.1, indicating that the coexistence of N vacancy and celestite can further inhibit the recombination of electrons and holes.

Based on the UV-vis absorption curves and fluorescence emission spectra analyzed above, the ranking of photocurrent intensity was established as CNSr-0.1 > Nv- $\text{g-C}_3\text{N}_4$  > celestite/ $\text{g-C}_3\text{N}_4$  >  $\text{g-C}_3\text{N}_4$ .

However, the photocurrent intensity of Nv- $\text{g-C}_3\text{N}_4$  was found to be smaller than that of  $\text{g-C}_3\text{N}_4$  when tests were performed (Fig. 7e). This result can be explained by our previous finding that photoelectrons can be captured and confined by N vacancy. As shown in Fig. 7e, a single celestite can only slightly improve the photocurrent intensity of  $\text{g-C}_3\text{N}_4$ . This slight change is consistent with the observed influence of a single celestite on the NO removal activity and fluorescence emission peaks of  $\text{g-C}_3\text{N}_4$ . Although both N vacancy and celestite do not greatly increase the photocurrent of  $\text{g-C}_3\text{N}_4$ , the coexistence of N vacancy and celestite significantly improves the photocurrent of  $\text{g-C}_3\text{N}_4$ . This suggests that the nature of the synergistic effects of celestite and N vacancy may be that celestite can release the photoelectrons which are confined by N vacancy (Fig. 7f).

Previous reports have established that modification of  $\text{Fe}^{3+}$  can

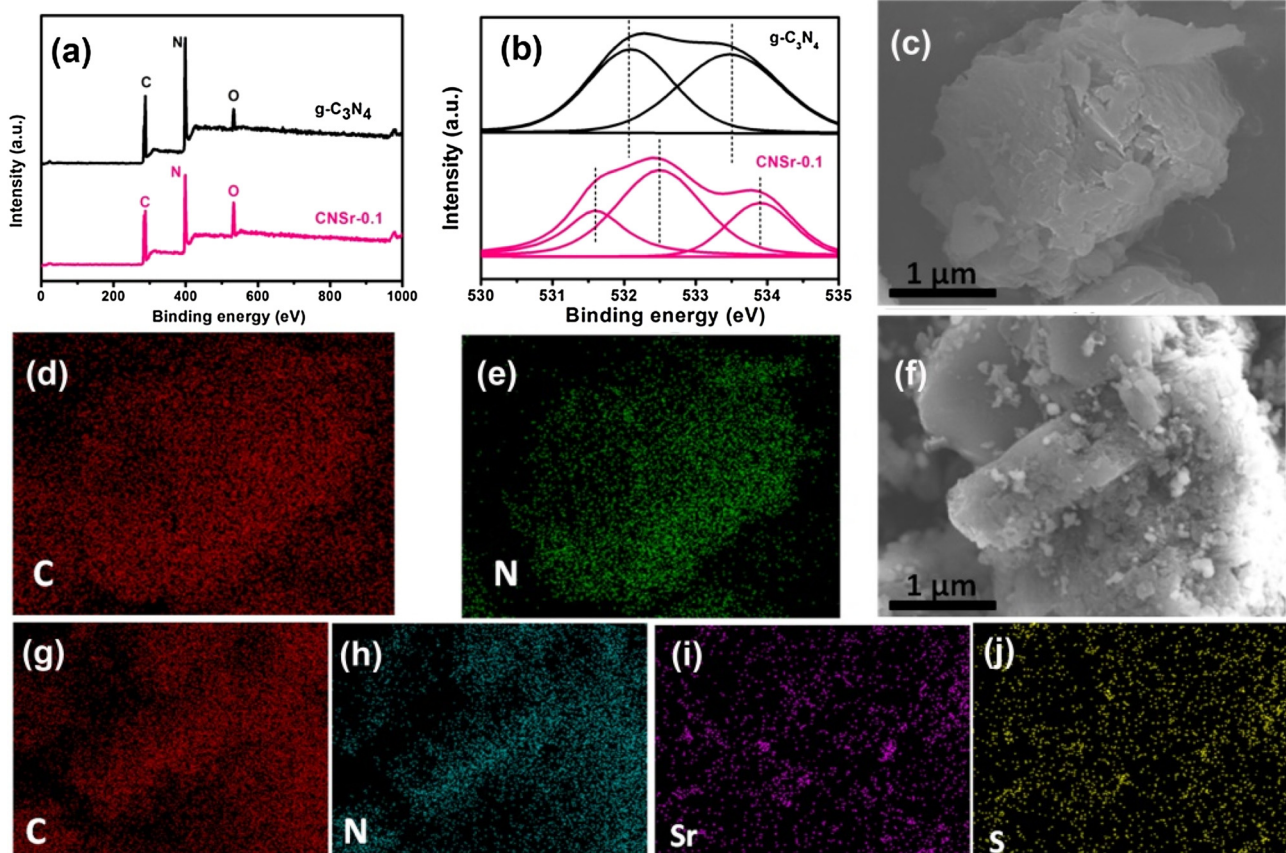


**Fig. 5.** (a) The whole XPS spectra of  $\text{g-C}_3\text{N}_4$  and CNSr-0.1; (b) the O1s XPS spectra of  $\text{g-C}_3\text{N}_4$  and CNSr-0.1 samples; (c) the SEM image, (d) C elements mapping, and (e) N elements mapping images of  $\text{g-C}_3\text{N}_4$ ; (f) the SEM image, (g) C elements mapping, (h) N elements mapping, (i) Sr elements mapping, and (j) S elements mapping images of CNSr-0.1.

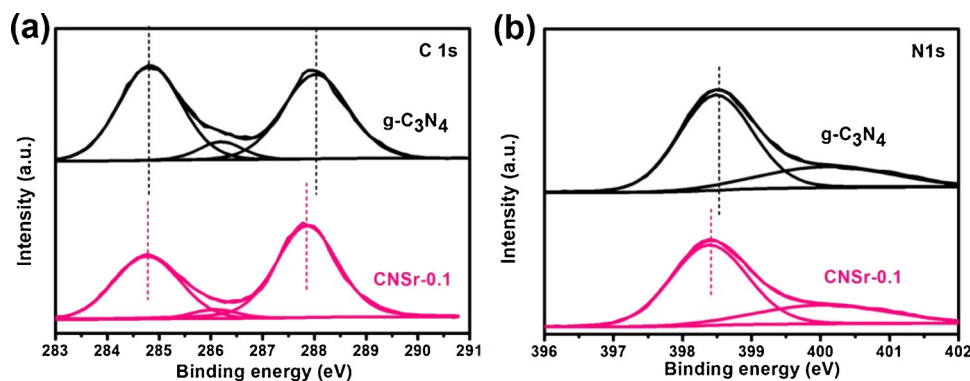


Fig. 6. (a) The C 1s XPS spectra of g-C<sub>3</sub>N<sub>4</sub> and CNSr-0.1; (b) The N 1s XPS spectra of g-C<sub>3</sub>N<sub>4</sub> and CNSr-0.1.

improve the separation efficiency of photo-generated electron-hole pairs [17], as the electrons from the photocatalyst conduction band can reduce Fe<sup>3+</sup> to Fe<sup>2+</sup>. As with Fe<sup>3+</sup>, Sr<sup>2+</sup> is also a variable valence metal ion. Therefore, it can be proposed that the reason celestite releases the photoelectrons confined by N vacancy, is related to Sr<sup>2+</sup>, which may extract the photo-generated electrons (-1.4 V) and be reduced to Sr<sup>°</sup> (-1.28 V, the test process can be found in supporting information.). To test this theory, H<sub>2</sub>SO<sub>4</sub> was used instead of celestite to synthesize a new sample (CN-H<sub>2</sub>SO<sub>4</sub>). However, the photocurrent

density of CN-H<sub>2</sub>SO<sub>4</sub> was not found to be stronger than that of g-C<sub>3</sub>N<sub>4</sub> (Fig. 7g), suggesting the importance of Sr<sup>2+</sup>. Additionally, X-ray photoelectron spectroscopy (XPS) was performed to compare the Sr 3d spectra of CNSr-0.1 and pre- and post- NO removal (Fig. 7h). Compared with CNSr-0.1, the used CNSr-0.1 sample exhibited a new Sr 3d peak at 132.1 eV, which can be assigned to Sr<sup>°</sup>, confirming that Sr<sup>2+</sup> can extract photo-generated electrons and be reduced to Sr<sup>°</sup>. The significant improvement in photocurrent density suggests that Sr<sup>°</sup> doesn't store these photo-generated electrons and that it can transfer the electrons to some

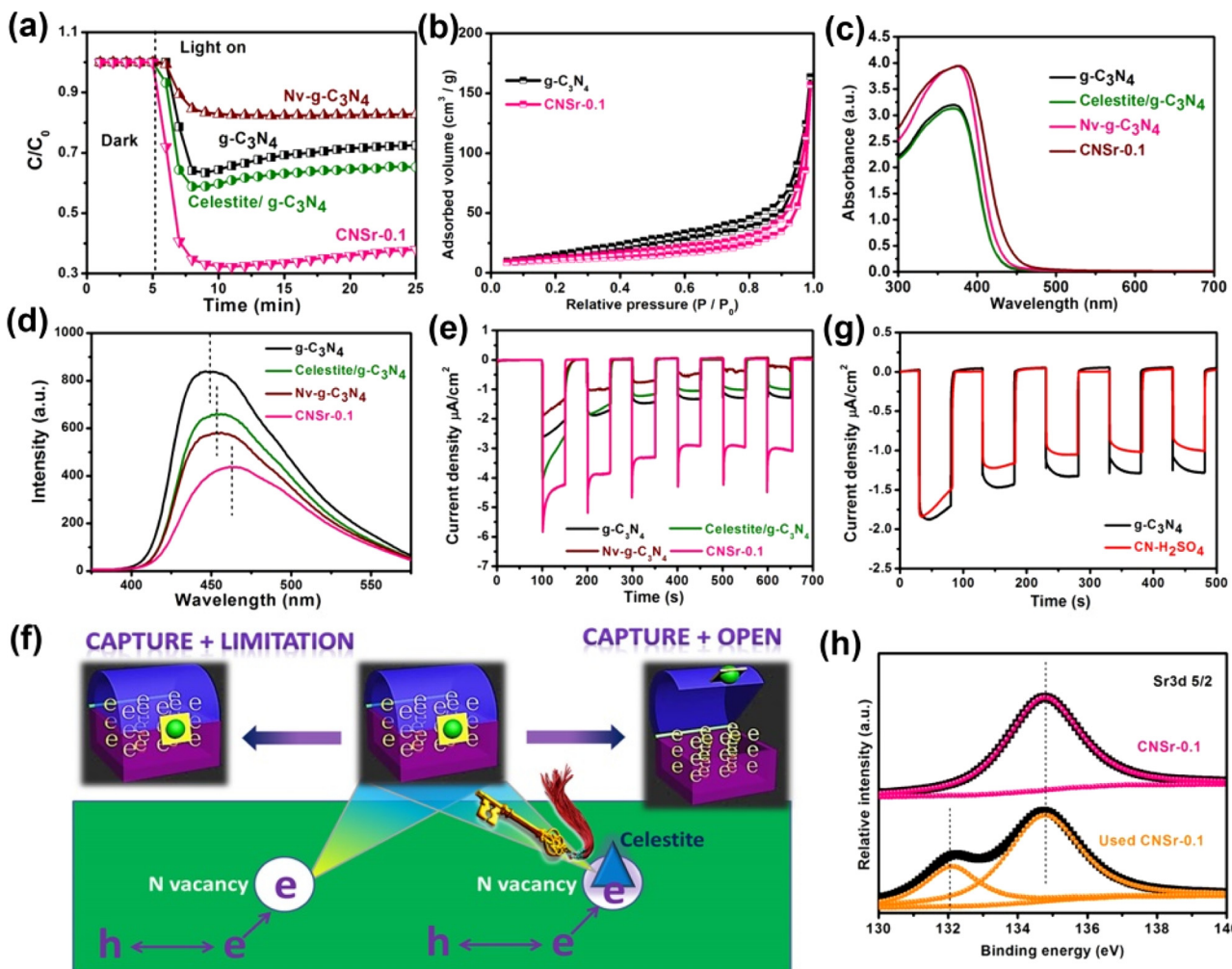
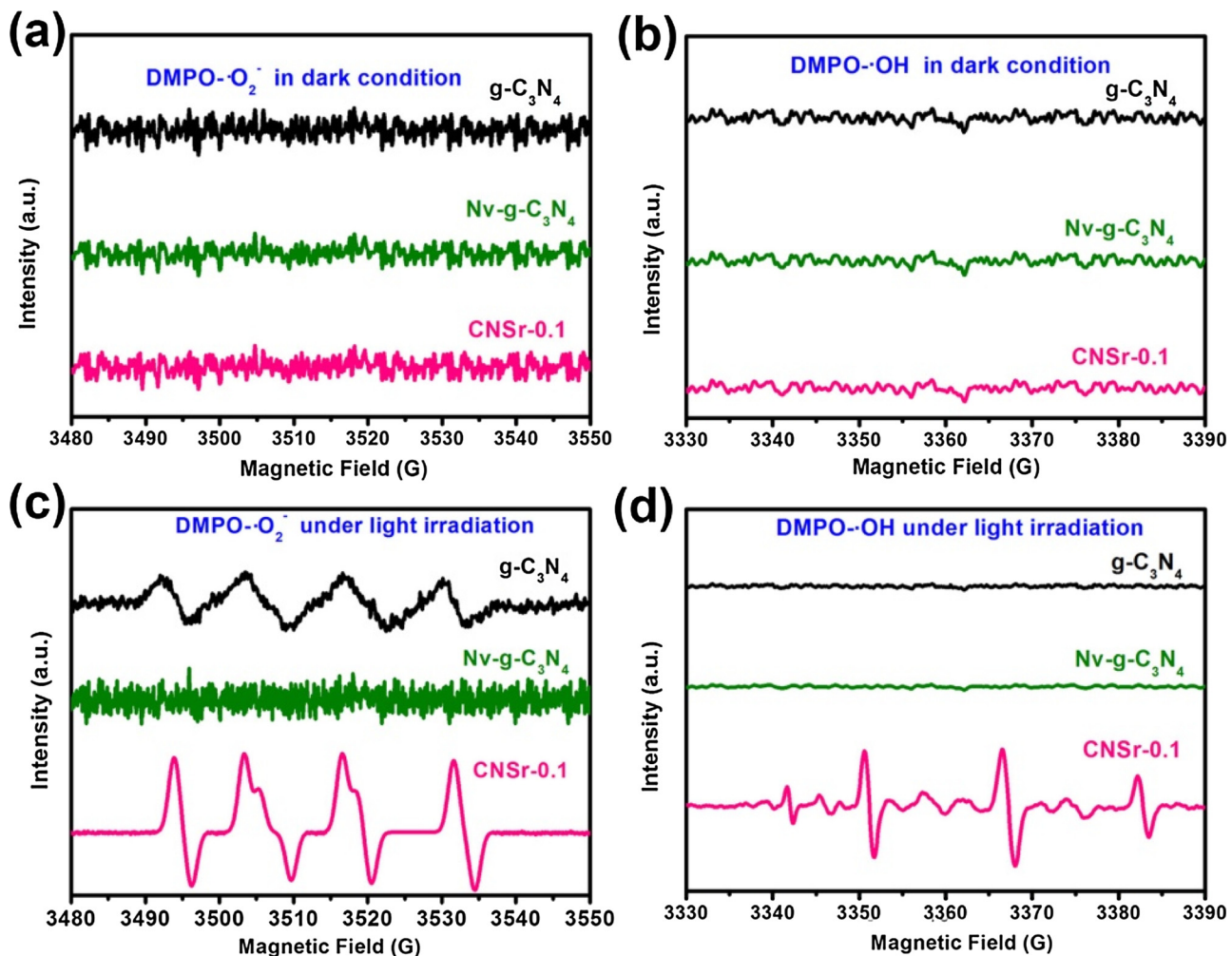
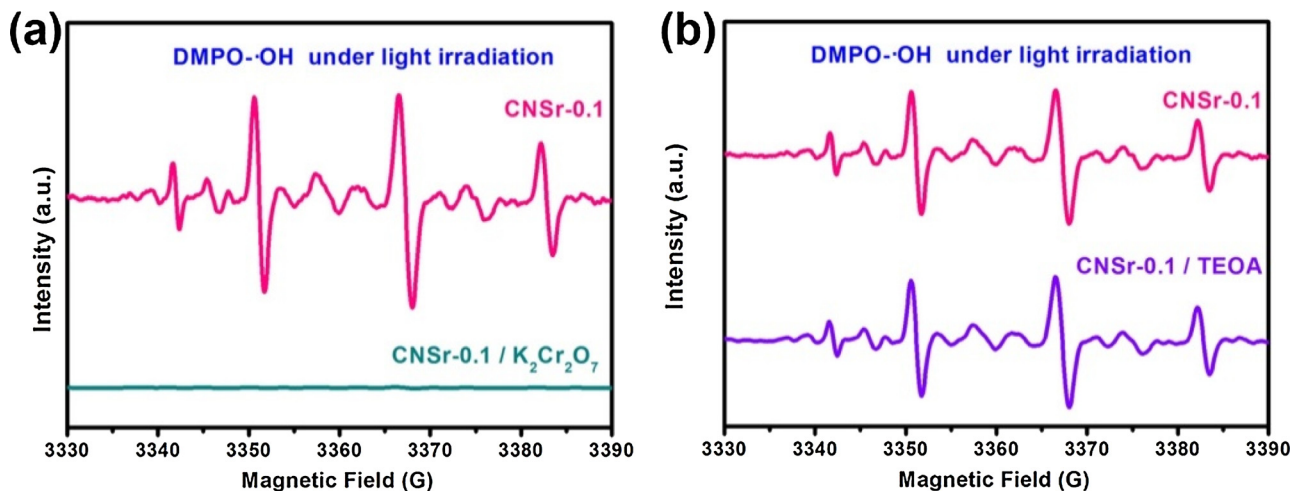


Fig. 7. (a) NO removal experiments in different systems; (b) the BET specific surface area of g-C<sub>3</sub>N<sub>4</sub> and CNSr-0.1; (c) UV-vis absorption spectra of different samples; (d) fluorescence emission spectra of different samples; (e) photocurrent curves of different samples; (f) celestite can release the photoelectrons which are confined by N vacancy; (g) the photocurrent density of g-C<sub>3</sub>N<sub>4</sub> and CN-H<sub>2</sub>SO<sub>4</sub>; (h) Sr 3d spectra of CNSr-0.1 and pre- and post- NO removal.



**Fig. 8.** Under dark conditions, no  $\cdot\text{OH}$  (a) or  $\cdot\text{O}_2^-$  (b) signals could be detected in any of the  $\text{g-C}_3\text{N}_4$ ,  $\text{Nv-g-C}_3\text{N}_4$  and  $\text{CNSr-0.1}$  systems; the production of  $\cdot\text{OH}$  (c) and  $\cdot\text{O}_2^-$  (d) under light irradiation.



**Fig. 9.** The production of  $\cdot\text{OH}$  (a) and  $\cdot\text{O}_2^-$  (b) under light irradiation in different systems.

kind of adsorbate, which will return  $\text{Sr}^\circ$  to  $\text{Sr}^{2+}$ .

To further understand the NO removal process, DMPO was employed to detect  $\cdot\text{O}_2^-$  and  $\cdot\text{OH}$  radicals. Under dark conditions, no  $\cdot\text{OH}$  or  $\cdot\text{O}_2^-$  signals could be detected in any of the  $\text{g-C}_3\text{N}_4$ ,  $\text{Nv-g-C}_3\text{N}_4$  and  $\text{CNSr-0.1}$  systems (Fig. 8a and b). With light illumination, neither  $\cdot\text{OH}$  or  $\cdot\text{O}_2^-$  could be detected in the  $\text{Nv-g-C}_3\text{N}_4$  system, consistent with the

conclusion that photoelectrons can be effectively captured and confined by N vacancy (Fig. 8c and d). Meanwhile, only a trace level of  $\cdot\text{O}_2^-$  could be detected in the  $\text{g-C}_3\text{N}_4$  system, corresponding to the low NO removal activity observed for this catalyst. In the  $\text{CNSr-0.1}$  system, both  $\cdot\text{OH}$  and  $\cdot\text{O}_2^-$  could be detected, with higher levels of  $\cdot\text{O}_2^-$  detected in the  $\text{CNSr-0.1}$  system than in the  $\text{g-C}_3\text{N}_4$  system. This increased amount

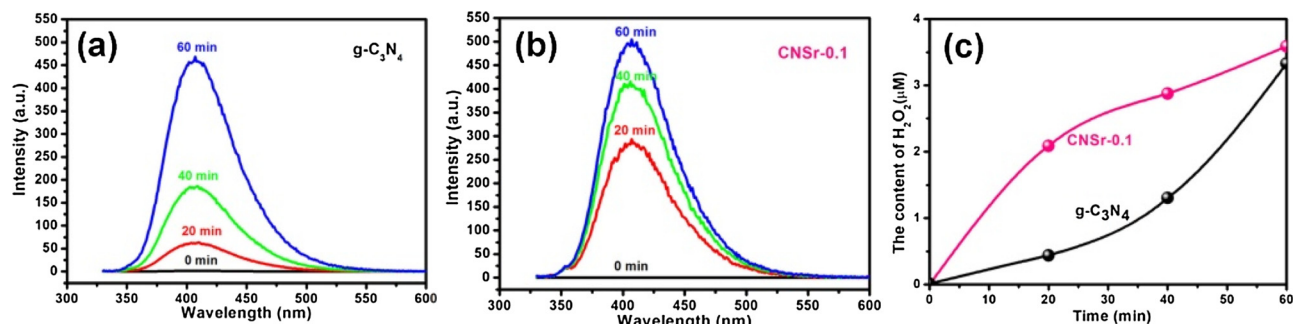


Fig. 10. The generation of H<sub>2</sub>O<sub>2</sub> in g-C<sub>3</sub>N<sub>4</sub> (a, c) and CNSr-0.1 (b, c) systems. (Detected by the Hitachi F7000).

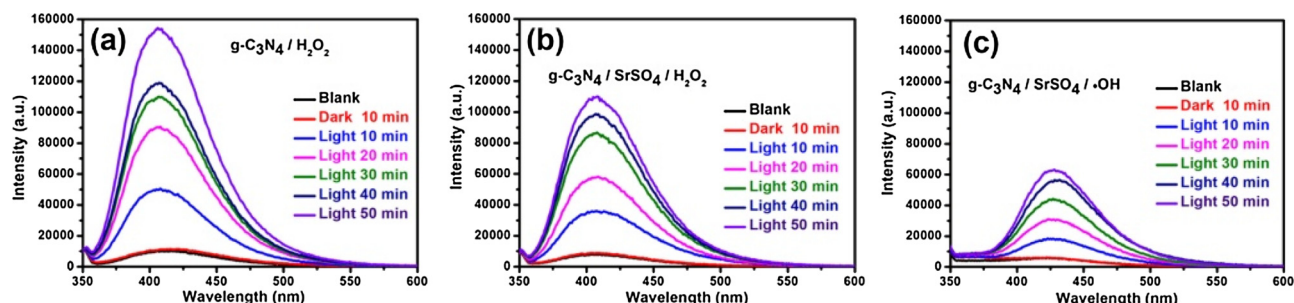


Fig. 11. The generation of H<sub>2</sub>O<sub>2</sub> in g-C<sub>3</sub>N<sub>4</sub> (a) and g-C<sub>3</sub>N<sub>4</sub> / SrSO<sub>4</sub> (b) systems; the generation of ·OH in g-C<sub>3</sub>N<sub>4</sub> / SrSO<sub>4</sub> (c) systems. (Detected by Edinburgh FS5).

of 'O<sub>2</sub><sup>-</sup> verifies that celestite can release the photoelectrons which are confined by N vacancy and that celestite can enhance the yield of ·OH radicals.

Based on previous reports, ·OH may be generated through either single-electron reduction ('O<sub>2</sub><sup>-</sup> → H<sub>2</sub>O<sub>2</sub> → ·OH) or by one-step hole oxidization (H<sub>2</sub>O → ·OH) [22,23]. To clarify the route of ·OH production in CNSr-0.1, hole and electron trapping experiments were carried out, with ·OH detection (Fig. 9). When potassium dichromate was added, ·OH signals in the CNSr-0.1 system became undetectable, while the addition of TEOA did not influence the level of ·OH detectable, confirming that ·OH was generated through single-electron reduction. As the single-electron reduction route is required for the generation of H<sub>2</sub>O<sub>2</sub>, the (p-hydroxyphenyl) acetic acid (POHPAA) analysis method was employed to measure H<sub>2</sub>O<sub>2</sub> levels during photocatalysis. As shown in Fig. 10, the generation of H<sub>2</sub>O<sub>2</sub> in the g-C<sub>3</sub>N<sub>4</sub> system was slower initially, then becoming more rapid (Fig. 10a and c), while the generation of H<sub>2</sub>O<sub>2</sub> in the CNSr-0.1 system followed a reverse process (Fig. 10b and c). This phenomenon suggests that both g-C<sub>3</sub>N<sub>4</sub> and CNSr-0.1 can produce H<sub>2</sub>O<sub>2</sub> during photocatalysis. However, combined with the ·OH generation observed in different sample systems, findings suggest that H<sub>2</sub>O<sub>2</sub> can be reduced to ·OH on the surface of CNSr-0.1, but not on the surface of g-C<sub>3</sub>N<sub>4</sub>. As noted previously, Sr<sup>2+</sup> can capture photo-generated electrons and be reduced to Sr<sup>°</sup>. Since the standard electrode potential of H<sub>2</sub>O<sub>2</sub>/·OH (-1.17 eV) is higher than that of Sr<sup>2+</sup>/Sr<sup>°</sup>, H<sub>2</sub>O<sub>2</sub> may restore Sr<sup>°</sup> to Sr<sup>2+</sup> via a Fenton like reaction (Sr<sup>°</sup> + H<sub>2</sub>O<sub>2</sub> → Sr<sup>2+</sup> + ·OH + OH<sup>-</sup>). Therefore, it may be speculated that this Fenton like reaction, driven by Sr<sup>°</sup>, is the mechanism by which celestite can enhance the yield of ·OH. To test this theory, the effect of SrSO<sub>4</sub> on H<sub>2</sub>O<sub>2</sub> generation by g-C<sub>3</sub>N<sub>4</sub> was assessed. As shown in Fig. 11, H<sub>2</sub>O<sub>2</sub> generation by g-C<sub>3</sub>N<sub>4</sub> was inhibited when SrSO<sub>4</sub> was added and ·OH could be detected in the g-C<sub>3</sub>N<sub>4</sub> system. These results confirm that H<sub>2</sub>O<sub>2</sub> can be decomposed to ·OH by Sr<sup>°</sup> via a Fenton like reaction. As the oxidation ability of ·OH is far stronger than that of 'O<sub>2</sub><sup>-</sup>, the function of celestite in the facilitation of decomposition of H<sub>2</sub>O<sub>2</sub>, contributes to the excellent NO removal activity of CNSr-0.1.

#### 4. Conclusions

In summary, this study demonstrates that celestite modified g-C<sub>3</sub>N<sub>4</sub> exhibits highly enhanced photocatalytic activity for NO removal, under visible light irradiation. The introduction of an appropriate amount of celestite can improve the S<sub>BET</sub> which allows the catalytic material to adsorb and transfer more reactant, providing more active sites for the photocatalytic reaction. Furthermore, Sr<sup>2+</sup> ions are beneficial for the separation and transfer of photo-generated electrons and holes, promoting photocatalytic activity. Sr<sup>°</sup> can facilitate the generation of ·OH via a Fenton like reaction, with the increased level of ·OH contributing to improved oxidation ability and photocatalytic efficiency.

#### Acknowledgments

Financial support by the National Nature Science Foundation of China (Grant No. 21603271 and 21876104) and National Key Research and Development Program of China, (Grant No. 2017YFC0110202) are gratefully appreciated.

#### Appendix A. Supplementary data

Supplementary material related to this article can be found, in the online version, at doi:<https://doi.org/10.1016/j.apcatb.2019.01.013>.

#### References

- [1] L.B. Kreuzer, C.K.N. Patel, Nitric oxide air pollution: detection by optoacoustic spectroscopy, *Science* 173 (1971) 45–47.
- [2] Z.H. Ai, W.K. Ho, S.C. Lee, L.Z. Zhang, Efficient photocatalytic removal of NO in indoor air with hierarchical bismuth oxybromide nanoplate microspheres under visible light, *Environ. Sci. Technol.* 43 (2009) 4143–4150.
- [3] Y. Huang, Y.L. Liang, Y.F. Rao, D.D. Zhu, J.J. Cao, Z.X. Shen, W.K. Ho, S.C. Lee, Environment-Friendly carbon quantum dots/ZnFe<sub>2</sub>O<sub>4</sub> photocatalysts: characterization, biocompatibility, and mechanisms for NO removal, *Environ. Sci. Technol.* 51 (2017) 2924–2933.
- [4] G.H. Dong, D. Chen, J.M. Luo, Y.Q. Zhu, Y.B. Zeng, C.Y. Wang, Voids padding induced further enhancement in photocatalytic performance of porous graphene-like carbon nitride, *J. Hazard. Mater.* 335 (2017) 66–74.
- [5] B. Xiao, P.S. Wheatley, X.B. Zhao, A.J. Fletcher, S. Fox, A.G. Rossi, L.L. Megson, S. Bardiga, L. Regli, K.M. Thomas, R.E. Morris, High-capacity hydrogen and nitric

oxide adsorption and storage in a metal-organic framework, *J. Am. Chem. Soc.* 129 (2007) 1203–1209.

[6] F. Dong, Z.W. Zhao, An advanced semimetal–organic Bi spheres–g-C<sub>3</sub>N<sub>4</sub> nano-hybrid with SPR-Enhanced visible-light photocatalytic performance for NO Purification, *Environ. Sci. Technol.* 49 (2015) 12432–12440.

[7] Z.H. Ai, W.K. Ho, S.C. Lee, L.Z. Zhang, Efficient photocatalytic removal of NO in indoor air with hierarchical bismuth oxybromide nanoplate microspheres under visible light, *Environ. Sci. Technol.* 43 (2009) 4143–4150.

[8] S. Jin, G.H. Dong, J.M. Luo, F.Y. Ma, C.Y. Wang, Improved photocatalytic NO removal activity of SrTiO<sub>3</sub> by using SrCO<sub>3</sub> as a new co-catalyst, *Appl. Catal. B: Environ.* 227 (2018) 24–34.

[9] Y. Huang, Y. Gao, Q. Zhang, Y. Zhang, J.J. Cao, W.K. Ho, S.C. Lee, Biocompatible FeOOH-Carbon quantum dots nanocomposites for gaseous NO<sub>x</sub> removal under visible light: improved charge separation and high selectivity, *J. Hazard. Mater.* 354 (2018) 54–62.

[10] H. Li, H. Shang, X.M. Cao, Z.P. Yang, Z.H. Ai, L.Z. Zhang, Oxygen vacancies mediated complete visible light NO oxidation via side-on bridging superoxide radicals, *Environ. Sci. Technol.* 52 (2018) 8659–8665.

[11] X.C. Wang, K. Maeda, A. Thomas, K. Takanabe, G. Xin, J.M. Carlsson, K. Domen, M. Antonietti, A metal-free polymeric photocatalyst for hydrogen production from water under visible light, *Nat. Mater.* 8 (2009) 76–80.

[12] G.H. Moon, M. Fujitsuka, S. Kim, T. Majima, X.C. Wang, W. Choi, Eco-Friendly photochemical production of H<sub>2</sub>O<sub>2</sub> through O<sub>2</sub> reduction over carbon nitride frameworks incorporated with multiple heteroelements, *ACS Catal.* 7 (2017) 2886–2895.

[13] C.H. Choi, L.H. Lin, S. Gim, S. Lee, H. Kim, X.C. Wang, W. Choi, Polymeric carbon nitride with localized aluminum coordination sites as a durable and efficient photocatalyst for visible light utilization, *ACS Catal.* 8 (2018) 4241–4256.

[14] G.H. Dong, W.K. Ho, Y.H. Li, L.Z. Zhang, Facile synthesis of porous graphene-like carbon nitride (C<sub>6</sub>N<sub>9</sub>H<sub>3</sub>) with excellent photocatalytic activity for NO removal, *Appl. Catal. B: Environ.* 174 (2015) 477–485.

[15] G.H. Dong, Z.H. Ai, L.Z. Zhang, Efficient anoxic pollutant removal with oxygen functionalized graphitic carbon nitride under visible light, *RSC Adv.* 4 (2014) 5553–5560.

[16] Z. Yang, A.K. Bertram, K.C. Chou, Why do sulfuric acid coatings influence the ice nucleation properties of mineral dust particles in the atmosphere? *J. Phys. Chem. Lett.* 2 (2011) 1232–1236.

[17] Y.J. Cui, Z.X. Ding, P. Liu, M. Antonietti, X.Z. Fu, X.C. Wang, Metal-free activation of H<sub>2</sub>O<sub>2</sub> by g-C<sub>3</sub>N<sub>4</sub> under visible light irradiation for the degradation of organic pollutants, *Phys. Chem. Chem. Phys.* 14 (2012) 1455–1462.

[18] Y. Huang, D. Zhu, Q. Zhang, Y. Zhang, J.J. Cao, Z. Shen, W.K. Ho, S.C. Lee, Synthesis of a Bi<sub>2</sub>O<sub>3</sub>CO<sub>3</sub>/ZnFe<sub>2</sub>O<sub>4</sub> heterojunction with enhanced photocatalytic activity for visible light irradiation-induced NO removal, *Appl. Catal. B: Environ.* 234 (2018) 70–78.

[19] D. Bingol, S. Aydogen, S.S. Gultekin, Neural model for the leaching of celestite in sodium carbonate solution, *Chem. Eng. J.* 165 (2010) 617–624.

[20] G.H. Dong, L.P. Yang, F. Wang, L. Zang, C.Y. Wang, Removal of nitric oxide through visible light photocatalysis by g-C<sub>3</sub>N<sub>4</sub> modified with perylene imides, *ACS Catal.* 6 (2016) 6511–6519.

[21] G.H. Dong, L. Zang, C.Y. Wang, Carbon vacancy regulated photoreduction of NO to N<sub>2</sub> over ultrathin g-C<sub>3</sub>N<sub>4</sub> nanosheets, *Appl. Catal. B: Environ.* 218 (2017) 515–524.

[22] X. Ding, W.K. Ho, J. Shang, L.Z. Zhang, Self-doping promoted photocatalytic removal of NO under visible light with Bi<sub>2</sub>MoO<sub>6</sub>: indispensable role of superoxide ions, *Appl. Catal. B: Environ.* 182 (2016) 316–325.

[23] K. Su, Z.H. Ai, L.Z. Zhang, Efficient visible light driven photocatalytic degradation of pentachlorophenol with Bi<sub>2</sub>O<sub>3</sub>/TiO<sub>2-x</sub>B<sub>x</sub>, *J. Phys. Chem. C.* 116 (2012) 17118–17123.